Josephson junction of nodal superconductors with a Rashba and Ising spin-orbit coupling

Gal Cohen [1,*] Ranjani Seshadri [1,†] Maxim Khodas,[2,‡] and Dganit Meidan[1,3,§]
[1]*Department of Physics, Ben-Gurion University of the Negev, Beer-Sheva 84105, Israel*
[2]*Racah Institute of Physics, Hebrew University of Jerusalem, Jerusalem 91904, Israel*
[3]*Université Paris-Saclay, CNRS, Laboratoire de Physique des Solides, 91405 Orsay, France*

(Received 24 January 2024; revised 28 March 2024; accepted 29 March 2024; published 16 April 2024)

We study the effect of a Rashba spin-orbit coupling on the nodal superconducting phase of an Ising superconductor. Such nodal phase was predicted to occur when applying an in-plane field beyond the Pauli limit to a superconducting monolayer transition metal dichalcogenides (TMD). Generically, Rashba spin orbit is known to lift the chiral symmetry that protects the nodal points, resulting in a fully gapped phase. However, when the magnetic field is applied along the x direction, a residual vertical mirror symmetry protects a nodal crystalline phase. We study a single-band tight-binding model that captures the low-energy physics around the Γ pocket of monolayer TMD. We calculate the topological properties, the edge state structure, and the current phase relation in a Josephson junction geometry of the nodal crystalline phase. We show that while the nodal crystalline phase is characterized by localized edge modes on non-self-reflecting boundaries, the current phase relation exhibits a trivial 2π periodicity in the presence of Rashba spin-orbit coupling.

DOI: 10.1103/PhysRevB.109.165427

I. INTRODUCTION

Transition metal dichalcogenides (TMDs) such as $NbSe_2$ and MoS_2 have been proposed and experimentally confirmed to be an ideal platform for in-depth explorations for unconventional superconductivity—both intrinsic and externally induced [1–14].

More recently, cutting-edge advances in fabrication techniques have facilitated the engineering of layered systems from these TMDs where the constituent layers are held together by weak van der Waals force [15,16]. Here, some systems are found to retain their superconducting property even down to the monolayer limit [14,17–25].

Unlike their bulk counterparts, many monolayer and few-layer TMD's break inversion symmetry, thereby giving rise to a very strong Ising spin-orbit coupling (SOC) [9,14,15,17–21,26], which pins the electron spins perpendicular to the plane. The most remarkable consequence of this strong SOC is that superconductivity survives at high in-plane magnetic fields even beyond the Pauli critical limit [2,14,17,19,20,22,23,27–31].

It was proposed that the presence of an in-plane field can induce a topological transition into a nodal superconducting phase [3,7] protected by a combination of an effective time reversal and particle-hole symmetry. The nodal superconducting phase is expected to be accompanied by Majorana flat bands [32,33], indication of which have been reported [34,35], as well as distinct 4π periodic Josephson current for the transverse momenta in-between the nodal points [36].

In this paper we study the effect of Rashba SOC on the nodal superconducting phase, focusing on the boundary modes and the Josephson current phase relation. Rashba SOC is naturally present due to electronic gates and the presence of a substrate and can be tuned experimentally. The presence of Rashba SOC breaks the chiral symmetry that protects the nodal superconducting phase, and as a result, the nodal points are generally gapped. However, when the in-plane field is aligned along the x direction, a lower crystalline symmetry protects the nodal phase [37]. We study the boundary states in the crystalline phase as well as the current-phase relation in a Josephson-junction geometry. Our results indicate that while the vertical mirror symmetry protects exponentially localized states at the boundary transformed by the symmetry, the current phase relation exhibits a trivial 2π periodicity in the presence of Rashba SOC.

The plan of the paper is as follows. We begin in Sec. II with an analysis of the low-energy momentum-space Hamiltonian and its related symmetries. In Sec. III we introduce a toy model on a triangular lattice, which reduces to the continuum Hamiltonian close to the Γ point. We discuss the topological properties of this model with and without Rashba SOC and study the stability of the boundary modes in a ribbon geometry. The physics of a Josephson junction fabricated out of such a material is discussed in Sec. IV.

II. CONTINUUM MODEL

An Ising superconductor such as monolayer $NbSe_2$ subjected to an in-plane magnetic field of magnitude h, with a superconducting pairing Δ is governed by the following

*galao@post.bgu.ac.il
†ranjanis@post.bgu.ac.il
‡maxim.khodas@mail.huji.ac.il
§dganit@bgu.ac.il

Bogoliubov-de-Gennes (BdG) Hamiltonian:

$$\mathcal{H}(\mathbf{k}) = \xi(\mathbf{k})\tau^z + \lambda(\mathbf{k})\sigma^z - \alpha_R(k_x\tau^z\sigma^y - k_y\sigma^x) + h\cos\theta\tau^z\sigma^x + h\sin\theta\tau^0\sigma^y + \Re(\Delta)\tau^y\sigma^y + \Im(\Delta)\tau^x\sigma^y, \quad (1)$$

where $\xi(\mathbf{k}) = (k_x^2 + k_y^2)/2m - \mu$ is the kinetic energy term with μ being the chemical potential. The Ising SOC $\lambda(\mathbf{k}) = \lambda_I(k_x^3 - 3k_xk_y^2)$ is unique to this class of materials, and pins the electron spins perpendicular to the x–y plane. The form of $\lambda(\mathbf{k})$ is constrained by the crystalline symmetry point group D_{3h}, which includes a mirror reflection plane M_z (with normal along the z direction), a threefold rotational symmetry C_3 and a vertical mirror M_x (with normal along the x direction). The strong Ising SOC protects superconductivity in the presence of an in-plane magnetic field h, which can exceed the Pauli limit. The parameter θ denotes the angle the in-plane magnetic field makes with the x axis. α_R determines the strength of Rashba SOC, typically present in experimental setups, and can be tuned by gating or by appropriate choice of substrate.

In the absence of Rashba SOC, i.e., when $\alpha_R = 0$, the in-plane direction of h is immaterial. When $|h| > \Delta$ the BdG spectrum has twelve nodal points on the high symmetry Γ–M lines $k_x = 0, \pm\sqrt{3}$ along which the Ising SOC vanishes. This nodal superconducting phase is accompanied by the presence of Majorana flat bands [3,7,32,33], as well as an energy phase relation that depends on the momentum transverse to the current direction, with a 4π periodicity for the momenta lying between each pair of nodal points [36].

In this paper we analyze the effect of Rashba SOC on the nodal superconducting phase, the fate of its boundary modes, and the Josephson current phase relation. To this end, we work in a parameter regime where $h > |\Delta|$ and there are twelve nodal points in the absence of Rashba SOC.

Family of 1D Hamiltonians and symmetries

The origin of the nodal points can be understood by analyzing the family of 1D Hamiltonian obtained by setting k_y as a parameter, $\mathcal{H}^{(1D)}_{k_y}(k_x)$. In the absence of Rashba SOC, i.e., when $\alpha_R = 0$, this model has a particle-hole symmetry given by

$$C\mathcal{H}^{(1D)}_{k_y}(k_x)C^{-1} = -\mathcal{H}^{(1D)}_{k_y}(-k_x) \quad (2)$$

with $C = \tau^x\mathcal{K}$, where $\mathcal{K}$ denotes the complex conjugation operator.

While the magnetic field explicitly breaks time-reversal symmetry, the model has an emergent modified time-reversal (TR) symmetry,

$$T\mathcal{H}^{(1D)}_{k_y}(k_x)T^{-1} = \mathcal{H}^{(1D)}_{k_y}(-k_x) \quad (3)$$

with $T = \sigma^x\tau^z\mathcal{K} = \Theta M_z\tau_z$, which is a combination of time-reversal symmetry $\Theta = i\sigma_y\mathcal{K}$ and basal plane mirror symmetry M_z. The family of 1D Hamiltonians therefore lies in class BDI of the Altland-Zirnbauer classification [38,39]. The presence of the nodal points can therefore be understood as a series of topological phase transitions tuned by the parameter k_y as explained in Ref. [36]. Next, we introduce a Rashba SOC as given in Eq. (1), which consists of two parts. The first term $k_x\sigma^y\tau^z$ breaks the modified time-reversal symmetry T while the second term $k_y\sigma^x$ breaks particle-hole symmetry C of the effective 1D model, leaving $\mathcal{H}^{1D}_{k_y}$ in class A. However, when the field is oriented along the x axis, i.e., when $\theta = 0$, the system has a residual vertical mirror symmetry plane, defined by,

$$M_x\mathcal{H}^{(1D)}_{k_y}(k_x)M_x^{-1} = \mathcal{H}^{(1D)}_{k_y}(-k_x) \quad (4)$$

with $M_x = \sigma_x\tau_z$. We will show below that this 1D Hamiltonian realizes a crystalline insulating phase associated with gapless edge states, which are localized along the x direction and propagate along y direction.

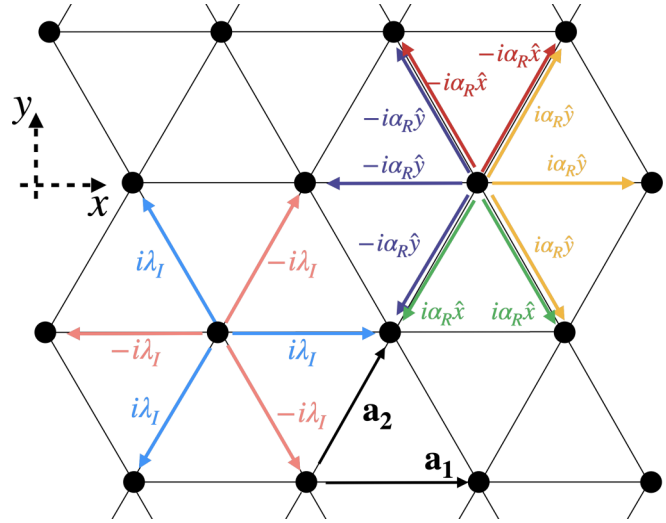

FIG. 1. Schematic diagram of the triangular lattice used for the tight-binding model showing the lattice vectors $\mathbf{a}_{1,2}$ and the hopping amplitudes corresponding to the Ising and Rashba SOC. This hopping profile results in the Hamiltonian H_I and H_R in Eqs. (6) and (9) respectively.

III. LATTICE MODEL

To gain further insight into the topological phase and the nature of its boundary modes, we study a tight-binding model presented in [8,40] that captures the key features of the topological superconducting phase and exhibits the same low-energy physics in the continuum limit $ka \to 0$. The lattice model consists of a nearest-neighbor hopping,

$$H_0 = -t\sum_{\langle i,j\rangle,s} c^\dagger_{i,s}c_{j,s} - \tilde{\mu}\sum_{i,s} c^\dagger_{i,s}c_{i,s},, \quad (5)$$

where $s = \uparrow, \downarrow$ denotes the spin, $\langle i, j\rangle$ spans all the nearest neighbors, and $\tilde{\mu}$ is the on-site chemical potential. In the continuum limit, $ka \to 0$, this reduces to the kinetic energy term $\xi(\mathbf{k})$ of Eq. (1) when we set $\tilde{\mu} = \mu - 6t$ and $t = 1/12m$. Similarly, Ising SOC is modeled as a nearest-neighbor hopping with alternating signs (shown in Fig. 1), that reflect the C_3 symmetry. Note that the sign is opposite for the two spins,

$$H_I = \frac{i\lambda_I}{2}\sum_{\langle i,j\rangle,s,s'} \nu_{ij}\sigma^z_{ss'}c^\dagger_{i,s}c_{j,s'} \quad (6)$$

where $\nu_{ij} = +1(-1)$ for $\mathbf{r}_{ij} = \mathbf{r}_i - \mathbf{r}_j = \mathbf{a}_1, -\mathbf{a}_2, \mathbf{a}_2 - \mathbf{a}_1 (-\mathbf{a}_1, \mathbf{a}_2, -\mathbf{a}_2 + \mathbf{a}_1)$, respectively, and the lattice vectors are: $\mathbf{a}_1 = (2a, 0)$ and $\mathbf{a}_2 = a(1, \sqrt{3})$.

The term arising due to the in-plane magnetic field ($\mathbf{h} = h_x, h_y$) is

$$H_B = \sum_{i,s,s'} (\mathbf{h} \cdot \boldsymbol{\sigma})_{ss'} c^\dagger_{i,s} c_{i,s'}, \tag{7}$$

while the term corresponding to superconductivity is given by

$$H_{SC} = \sum_i \Delta c^\dagger_{i,\downarrow} c^\dagger_{i,\uparrow} + \Delta^* c_{i,\uparrow} c_{i,\downarrow}. \tag{8}$$

Lastly, the Rashba term can be written as follows:

$$H_R = -\frac{i\alpha_R}{6} \sum_{\langle i,j\rangle,s,s'} \mathbf{z} \cdot (\mathbf{r}_{ij} \times \boldsymbol{\sigma})_{ss'} c^\dagger_{i,s} c_{j,s'}. \tag{9}$$

In momentum space the lattice Hamiltonian, Eqs. (5)–(9) take the following form:

$$\begin{aligned} H = &\sum_{\mathbf{k},s} \tilde{\xi}(\mathbf{k}) c^\dagger_{\mathbf{k}} c_{\mathbf{k}} - \sum_{\mathbf{k},ss'} \tilde{\lambda}_I(\mathbf{k}) \cdot \boldsymbol{\sigma}_{ss'} c^\dagger_{\mathbf{k}s} c_{\mathbf{k}s'} \\ &+ \sum_{\mathbf{k},ss'} \tilde{\alpha}_R(\mathbf{k}) \cdot \boldsymbol{\sigma}_{ss'} c^\dagger_{\mathbf{k}s} c_{\mathbf{k}s'} + \sum_{\mathbf{k},ss'} \mathbf{h} \cdot \boldsymbol{\sigma}_{ss'} c^\dagger_{\mathbf{k},s} c_{\mathbf{k},s'} \\ &+ \sum_{\mathbf{k},s,s'} i\Delta\sigma^y_{s,s'} c^\dagger_{\mathbf{k},s} c^\dagger_{-\mathbf{k},s'} + \text{H.c.} \end{aligned} \tag{10}$$

Here the kinetic energy term is

$$\tilde{\xi}(\mathbf{k}) = -4t \cos(k_x) \cos(\sqrt{3}k_y) - 2t \cos(2k_x) - \tilde{\mu}. \tag{11}$$

Here $\tilde{\lambda}_I(\mathbf{k})$ and $\tilde{\alpha}_R(\mathbf{k})$ correspond to the Ising and Rasbha SOCs respectively and have the following form in the lattice model:

$$\tilde{\lambda}_I(\mathbf{k}) = \lambda_I \hat{z}[\sin(\mathbf{k} \cdot \mathbf{a}_1) + \sin(\mathbf{k} \cdot (\mathbf{a}_2 - \mathbf{a}_1)) - \sin(\mathbf{k} \cdot \mathbf{a}_2)], \tag{12}$$

and

$$\begin{aligned} \tilde{\alpha}_R(\mathbf{k}) = &-\frac{\sqrt{3}\alpha_R}{2} \hat{x}[\sin(\mathbf{k} \cdot (\mathbf{a}_2 - \mathbf{a}_1)) + \sin(\mathbf{k} \cdot \mathbf{a}_2)] \\ &- \frac{\alpha_R}{2} \hat{y}[\sin(\mathbf{k} \cdot (\mathbf{a}_2 - \mathbf{a}_1)) - \sin(\mathbf{k} \cdot \mathbf{a}_2) \\ &- 2\sin(\mathbf{k} \cdot \mathbf{a}_1)] \end{aligned} \tag{13}$$

and we have taken the pairing term Δ to be real. The strength of each term is suitably chosen to give the same low-energy Hamiltonian as Eq. (1).

Figure 2 shows the dispersion of the two lower energy bands of the lattice model given by Eq. (10), in the vicinity of the Γ point. The Rashba SOC breaks the chiral symmetry thus generically lifting the nodal points resulting in a fully gapped phase. However, when the magnetic field is aligned along the x direction, the system has a residual vertical mirror symmetry M_x, which protects the nodal points along the $k_x = 0$ symmetry line. The system therefore realizes a nodal crystalline phase, as we show below. Due to the breaking of chiral symmetry, the nodes are shifted away from zero energy.

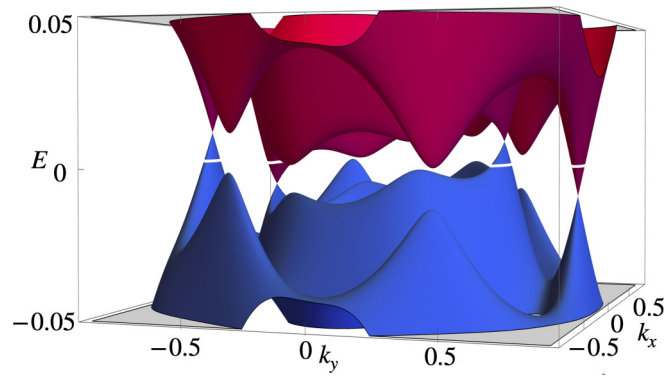

FIG. 2. Energy dispersion of the two low-energy bands of Eq. (10) in the vicinity of the Γ point. The parameters used are $m = 1$, $\tilde{\mu} = -0.3$, $\lambda_{SO} = 0.15$, $h = 0.1$, $\Delta = 0.06$, and $\alpha_R = 0.02$. The white line marks the zero-energy contour. The four gap-closing points are shifted away from the $E = 0$ plane and lie on the $k_x = 0$ line.

A. Symmetries and topological classification

To gain further insight into the topological aspects of the lattice model and the origin of the nodal points in the spectrum we consider the family of lattice 1D Hamiltonians obtained by treating k_y in Eq. (10) as a parameter.

As discussed in Sec. II, Rashba SOC lifts the chiral symmetry thus leaving the family of 1D lattice Hamiltonians in class A. However, when the magnetic field is aligned along the x direction the resulting 1D Hamiltonian is symmetric under vertical mirror M_x, and is gapped except for four discrete values of k_y. For values of k_y between these nodal points the system realizes a one-dimensional topological crystalline phase [41,42].

At $k_x^{(\text{inv})} = 0, \pi$, the 1D Hamiltonian is mapped onto itself under reflection. In these reflection symmetric momenta, the energy levels have a well-defined reflection eigenvalue. The reflection eigenvalues of the two occupied levels, labeled as 1, 2 are $\zeta_{1,2}(k_x = 0)$ and $\zeta_{1,2}(k_x = \pi)$ corresponding to $\Pi_{k_x=0} M_x \Pi_{k_x=0}$ and $\Pi_{k_x=\pi} M_x \Pi_{k_x=\pi}$, respectively, where Π_k is the projector onto the two lowest energy levels at a given momentum k. These are continuously connected to the negative energy states in the absence of Rashba SOC. The reflection eigenvalues define a $\mathbb{Z}_2$ index given by

$$\nu_{\mathcal{M}} = \prod_{i \in \text{occ}, k_x^{\text{inv}}} \zeta_i\left(k_x^{\text{inv}}\right). \tag{14}$$

Figure 3 shows the value of the reflection eigenvalues of the two occupied bands 1, 2 at the two reflection symmetric momenta, $k_x^{(\text{inv})} = 0, \pi$, as a function of parameter k_y. Solid and dashed gray lines indicate the spectra along the $k_x = 0$ and $k_x = \pi$ lines, respectively. The closing and reopening of the band gap is accompanied by a topological phase transition; i.e., a change in sign of $\zeta_1(\pi)$ (for the gap closing at $k_x = 0$) and $\zeta_2(0)$ (for the gap closing at $k_x = \pi$).

B. Bulk-boundary correspondence

To examine the bulk-boundary correspondence for the nodal crystalline phase, we study the tight-binding lattice

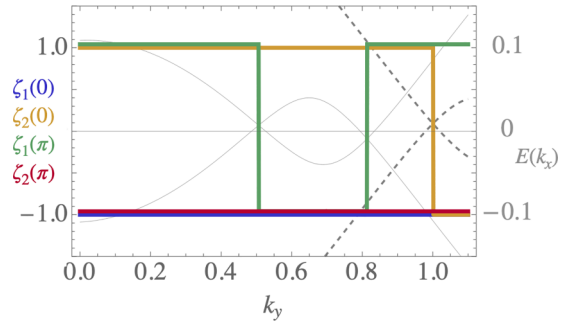

FIG. 3. The evolution of the mirror eigenvalues at the reflection symmetric momenta $k_x = 0, \pi$ of the two lowest energy levels for the lattice toy model. (The lines are shifted vertically for clarity.) The dispersion of the two low-energy bands at $k_x = 0$ ($k_x = \pi$) is shown in solid (dashed) gray lines, indicating the location of the nodal points. The parameters used are $m = 1$, $\tilde{\mu} = -0.3$, $\lambda_{SO} = 0.15$, $h = 0.1$, $\Delta = 0.06$, and $\alpha_R = 0.02$.

Hamiltonian on a ribbon-like geometry with open boundary conditions in the (non-self-reflecting) x direction, and periodic boundary conditions in the y direction. This makes k_y a good quantum number and allows us to write the Hamiltonian in the ribbon geometry as an effective $1D$ chain for a given k_y,

$$H_{\text{Rib}}(k_y) = H_0(k_y) + H_I(k_y) + H_R(k_y) + H_B + H_{SC}. \quad (15)$$

These terms correspond to kinetic energy, Ising SOC, Rashba SOC, in-plane field, and superconductivity respectively, a detailed expression is given in Appendix A.

Diagonalizing the Hamiltonian in Eq. (15), we obtain the eigenvalues and the corresponding wavefunctions for the bulk and edge states. Figure 4(a) shows the BdG spectrum in the Ribbon geometry for $\alpha_R = 0$. Eigenvalues corresponding to states localized on the open x direction boundary are shown in red. The two pairs of nodal points at $k_y \approx 0.25, 0.4$ and $k_y \approx 0.5, 0.8$ are accompanied by the appearance of zero-energy states, which are localized on the open x direction boundary (marked in red).

Figure 4(b) shows the BdG spectra for $\alpha_R = 0.01$. When the Rashba term is switched on, only one pair of nodal points survive, which are shifted away from zero energy. In Fig. 4(b) these are located at $k_y \approx 0.5$ and 0.8. The two degenerate midgap states connecting this pair of nodes (shown in red) live on the (non-self-reflecting) x boundary and have a nonzero dispersion as a function of k_y (the conjugate momenta for the direction parallel to the boundary). The degeneracy between the boundary mode is protected by the mirror symmetry M_x. In Appendix C we show that any perturbation breaking this reflection symmetry splits these edge states, see Fig. 3.

Figure 5 shows the spatial profile of the degenerate midgap states for a fixed $k_y = 0.75$ between the pairs of nodes, for different values of Rashba SOC (indicated by the markers). Here n_x indicates the position along the chain. Solid lines indicate a best fit to an exponential law $\psi(x) \approx \exp(-x/\xi)$, showing that the states remain exponentially localized even for finite α_R. Importantly, unlike the $\alpha_R = 0$ case, for finite $\alpha_R \neq 0$ the edge states do not satisfy the Majorana condition $\psi_b \neq (u_\uparrow, u_\downarrow, u_\uparrow^*, u_\downarrow^*)^T$. This observation is also consistent with the analytic derivation of the boundary mode in the continuum limit, see Appendix B. The inset in Fig. 5 shows the best fit of the decay length with increasing Rashba SOC.

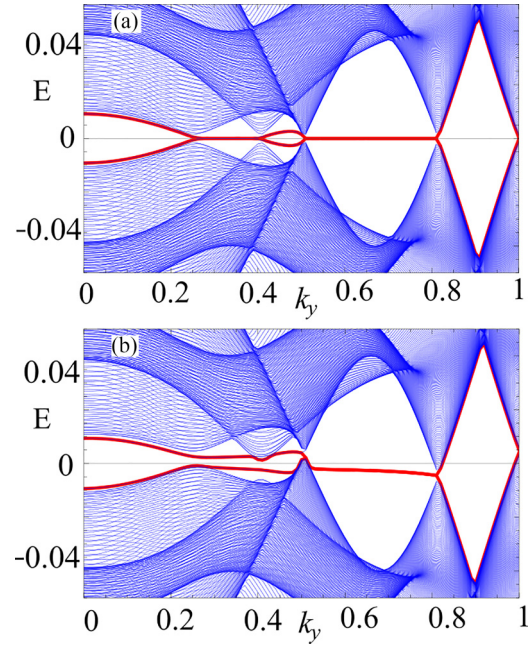

FIG. 4. Energy spectrum for a nanoribbon with open boundary conditions for (a) $\alpha_R = 0$ and (b) $\alpha_R = 0.01$ obtained by diagonalizing Eq. (15). The Rashba SOC breaks chiral symmetry and moves the nodal points away from zero energy. Midgap states localized at the open boundaries of the ribbon are marked in red. These states decay exponentially into the bulk for momenta k_y between pairs of nodal points.

IV. JOSEPHSON JUNCTION

The presence of the zero-energy boundary modes is known to affect the energy and current across a tunnel junction between two superconductors. A Josephson junction consists of two superconductors separated by a weak link such as an insulator or a weaker/nonsuperconducting material. The energy of the tunnel junction depends on the phase difference between

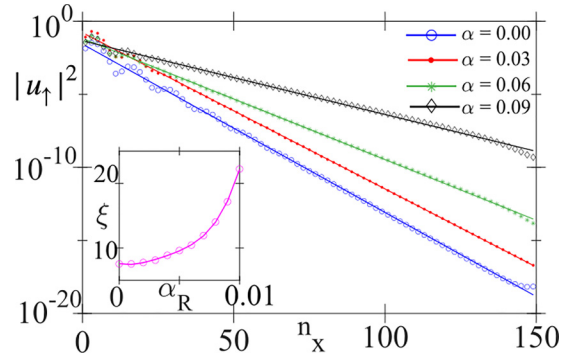

FIG. 5. Semi-log plot of the decay length of the "particle up" component $|u_\uparrow|^2$ of the edge-state spinor as a function of position at momentum $k_y \approx 0.75$ for different values of Rashba SOC strength α_R, while keeping all the other parameters unchanged. Here the parameters are $m = 1, \tilde{\mu} = -0.3, \lambda_I = 0.15, h = 0.1$, and $\Delta = 0.06$.

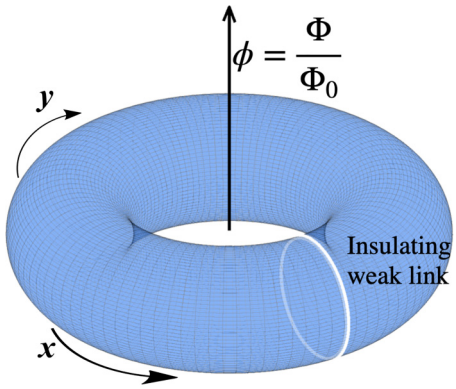

FIG. 6. Schematic showing the torus geometry used to study the Josephson junction. The y direction has periodic boundary conditions, making k_y a good quantum number. The change in the phase of the superconducting pairing corresponds to a flux Φ through this torus. The 1D chain along the x direction has twisted boundary conditions, i.e., all hopping parameters across the insulating weak link shown in white, acquire a phase $\phi = \Phi/\Phi_0$, Φ_0 being the flux quantum, and are attenuated by a factor proportional to the strength of the insulating barrier.

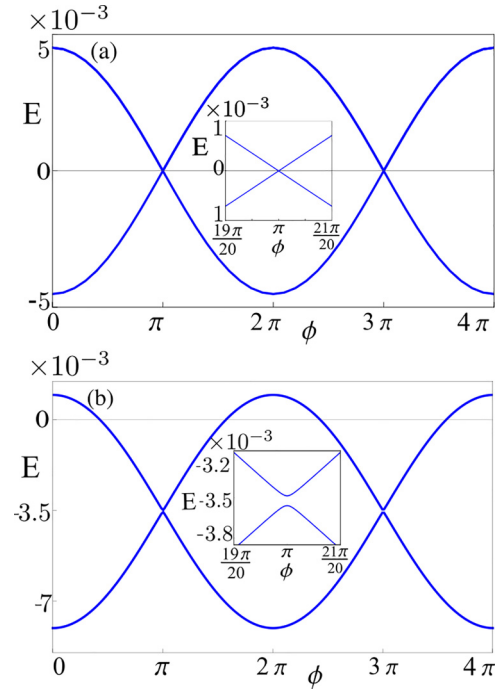

FIG. 7. Energy-phase relation of a Josephson junction obtained by solving the lattice model on a torus geometry of Fig. 6. The Rashba SOC is (a) $\alpha_R = 0$ and (b) $\alpha_R = 0.01$. We have chosen the momentum $k_y = 0.75$, which lies between two nodal points. In (a) we find that there are zero crossings at $\phi = \pi, 3\pi$ as is clear from the inset. This means $E_J(\phi)$ has a 4π periodicity. However in (b) the Josephson energy-phase relation is no longer symmetric about $E = 0$. Additionally, there is no crossing at $\phi = \pi, 3\pi$ and therefore only a 2π periodicity in $E(\phi)$, the parameters are $m = 1$, $\tilde{\mu} = -0.3$, $\lambda_I = 0.15$, $h = 0.1$, and $\Delta = 0.06$

the two superconductors, with a periodicity of 2π. This periodicity reflects the fact that only Cooper pairs of charge $2e$ can tunnel across the junction. The situation changes when the junction consists of topological superconductors. The presence of gapless Majorana zero modes at their ends facilitates the tunneling of single electrons, leading to a doubling of the periodicity to 4π [43–45]. When the junction is made up of nodal superconductors, the current phase relation depends on the orientation of the junction and the momentum transverse to the current direction [36].

To study the Josephson energy-phase relation we close the finite ribbon into a torus-like geometry by adding a weak link between the first and last sites of the effective 1D chain, see Fig. 6. All hopping terms across the weak link acquire a phase ϕ and are also attenuated by a factor proportional to the strength of the insulating barrier. Varying the phase difference ϕ across the junction for a given k_y allows to obtain the energy phase relation.

Figure 7 shows $E(\phi)$ for the midgap states at a fixed $k_y = 0.76$ that lie between pair of nodal points. For $\alpha_R = 0$ this value of $k_y = 0.76$ corresponds to a topological nontrivial phase of class BDI with winding $W = 1$. Conversely, with $\alpha_R \neq 0$ this k_y value corresponds to a crystalline topological phase with $\nu_{\mathcal{M}} = -1$, see Fig. 3. In the absence of Rashba SOC, shown in Fig. 7(a), the Josephson energy exhibits a 4π periodicity similar to the continuous model studied in Ref. [36], with the energy levels crossing zero at $\phi = \pi$ and 3π. This indicates the presence of Majorana edge states localized in the vicinity of the weak link, which decay exponentially into the bulk. Note that Fig. 7 shows the current-phase relation for the low-energy state only. All higher energy states follow a 2π periodicity.

When the Rashba SOC is finite, shown in Fig. 7(b), we find that $E(\phi)$ is no longer symmetric about the $E = 0$ line, i.e., it is shifted away from zero. Moreover, an energy gap opens at $\phi = \pi$, 3π in the presence of a Rashba SOC as is clear from the inset in Fig. 7(b). Hence, in the presence of Rashba SOC the Josephson energy-phase relation has a 2π periodicity for all k_y values. This is consistent with the observation that the exponentially localized boundary states are not Majorana modes.

V. CONCLUSIONS

We have studied the effect of Rashba spin-orbit coupling on the nodal superconducting phase of an Ising superconductor. This nodal phase was predicted in monolayer TMD's such as $NbSe_2$ in the presence of an in-plane field, which exceeds the Pauli limit $|h| > \Delta$ [3,7]. The presence of Rashba SOC breaks the chiral symmetry and generally lifts the nodal points, resulting in a fully gapped state. However, when the magnetic field is aligned along the x direction line the system has a residual mirror symmetry M_x, which protects the nodal points at $k_x = 0$. The system therefore realizes a nodal crystalline phase, characterized by states exponentially localized at the (non-self-reflecting) x boundary, which disperse parallel to the boundary, provided that the x boundary preserves the crystalline symmetry. However, we find that even in the presence of exponentially localized boundary states, the current phase relation in a Josephson junction becomes trivial and follows a 2π periodicity.

We note that Rashba spin-orbit coupling is typically present in experimental setups and can be controlled using gates and by changing substrates. This gives an experimental knob to tune in and out of the topological phase, thus changing the 4π periodic current phase relation to the trivial 2π.

ACKNOWLEDGMENTS

The authors would like to thank Hadar Steinberg and Ganapathy Murthy for fruitful discussions. D.M. acknowledges support from the Israel Science Foundation (ISF) (Grant No. 1884/18). M.K. and D.M. acknowledge support from the ISF (Grant No. 1251/19).

APPENDIX A: EFFECTIVE HAMILTONIAN FOR A 1D CHAIN

We study the tight-binding lattice Hamiltonian in a ribbon-like geometry with open boundary conditions in the x direction and periodic boundary conditions in the y direction. Treating k_y as a parameter, the resulting model describes a family of 1D chains along the x direction. Below we setting the lattice parameter $a = 1$. The resulting family of 1D chains is described by (15) with the terms corresponding to kinetic energy $\mathcal{H}_0$, Ising SOC $\mathcal{H}_I$ and Rashba SOC $\mathcal{H}_R$ are all dependent on k_y, and involve terms, which couple nearest as well as next-nearest neighbors,

$$H_0(k_y) = 2t\cos(\sqrt{3}k_y)\sum_{i,\sigma} c^\dagger_{i+1,\sigma}c_{i,\sigma} + \text{H.c.} + t\sum_{i,\sigma} c^\dagger_{i+2,\sigma}c_{i,\sigma} + \text{H.c.} - \tilde{\mu}\sum_{i,\sigma} c^\dagger_{i,\sigma}c_{i,\sigma}, \quad \text{(A1)}$$

$$H_I(k_y) = -2i\lambda_I\cos(\sqrt{3}k_y)\sum_{i,\alpha,\beta} c^\dagger_{i+1,\alpha}\sigma^z_{\alpha\beta}c_{i,\beta} + \text{H.c.} + i\lambda_I\sum_{i,\alpha,\beta} c^\dagger_{i+2,\alpha}\sigma^z_{\alpha\beta}c_{i,\beta} + \text{H.c.}, \quad \text{(A2)}$$

$$H_R(k_y) = -\frac{\alpha_R}{2\sqrt{3}}\sin(\sqrt{3}k_y)\sum_{i,\alpha,\beta} c^\dagger_{i+1,\alpha}\sigma^x_{\alpha\beta}c_{i,\beta} + \text{H.c.} + i\frac{\alpha_R}{6}\cos(\sqrt{3}k_y)\sum_{i,\alpha,\beta}\left[c^\dagger_{i+1,\alpha}\sigma^y_{\alpha\beta}c_{i,\beta} + c^\dagger_{i+2,\alpha}\sigma^y_{\alpha\beta}c_{i,\beta} + \text{H.c.}\right]. \quad \text{(A3)}$$

The in-plane magnetic field arises from on-site terms,

$$H_B = \sum_{i,\alpha,\beta}(\mathbf{h}\cdot\boldsymbol{\sigma})_{\alpha,\beta}c^\dagger_{i,\alpha}c_{i,\beta}. \quad \text{(A4)}$$

Note that in all the terms above, we have suppressed the index k_y for the creation (annihilation) operators. However, since the superconducting term couples particle and hole components, it is written as

$$H_{SC} = \sum_i \Delta c^\dagger_{i,k_y\uparrow}c^\dagger_{i,-k_y,\downarrow} + \text{H.c.} \quad \text{(A5)}$$

The Hamiltonian in Eq. (15) is used to obtain the excitation spectrum in Figs. 5 and 9 (see below), as well as the Josephson current phase relation Fig. 7.

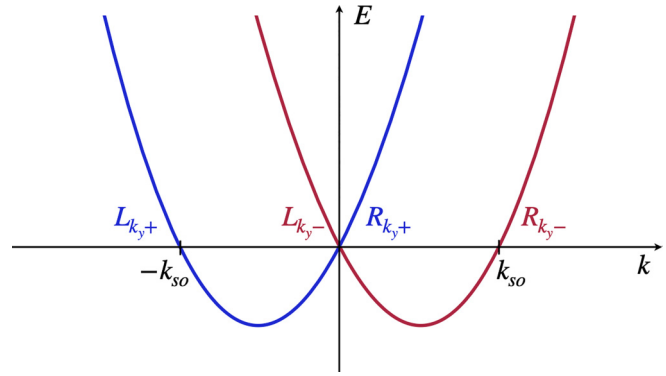

FIG. 8. Spectrum of the bare 1D effective Hamiltonian Eq. (B1) consists of two spin-orbit bands (marked by $\pm$) that cross the Fermi level $\mu_{k_y} = 0$ at the Fermi momenta $k_F = 0, \pm k_{so}$.

APPENDIX B: DERIVATION OF BOUNDARY MODES IN THE CONTINUUM LIMIT OF THE EFFECTIVE 1D MODEL

In this Appendix, we study the boundary modes present in the nodal crystalline phase when an in-plane magnetic field is applied along the x direction. The analysis is done in the continuum limit of the effective 1D Hamiltonian obtained from (1) by treating k_y as a parameter. To analyze the wave function of the boundary modes, we focus on the k_y values that lie between the remaining nodal points along the $\Gamma - M$ line (along $k_x = 0$). For this regime of parameters, the Ising spin-orbit coupling ϵ_{I-SO} is the largest energy scale $\epsilon_{I-SO} \gg h, \Delta, \epsilon_{R-SO}, \mu_{k_y}$. Working in this regime allows us to linearize the spectrum around the Fermi points determined by the Ising spin-orbit coupling and treat the magnetic field, superconductivity, and Rashba SOC as weak perturbations.

Following a similar analysis as in Ref. [46], we consider initially the following bare Hamiltonian:

$$\mathcal{H}_0^{1D}(k) = \frac{k^2}{2m} - \mu_{k_y} + \lambda_I k\left(k^2 - 3k_y^2\right)\sigma^z + \alpha_R(k\sigma^y) \quad \text{(B1)}$$

setting aside the gap-opening terms such as magnetic field, SC, and the transverse Rashba term. Here $k \equiv k_x$ is the momentum of the 1D system and the Pauli matrices σ operate on the spin basis. For simplicity we consider the k_y for which $\mu_{k_y} = 0$.

The eigenvalues of the bare 1D Hamiltonian (B1) are given by

$$E(k) = \frac{k^2}{2m} \pm k\sqrt{\alpha_R^2 + \lambda^2\left(k^2 - 3k_y^2\right)^2}, \quad \text{(B2)}$$

and the Fermi points that satisfy $ka \ll 1$ are located at $k = 0$ and $k_{so} = \pm\sqrt{3k_y^2 - \frac{\sqrt{16\lambda^2m^2(3k_y^2 - 4\alpha_R^2m^2)+1}-1}{8\lambda^2m^2}}$. Figure 8 shows the spectrum of the bare Hamiltonian in the limit $ka \ll 1$. In addition, we have three gap-opening perturbations,

$$\mathcal{H}_z = h\int_x \Psi_{k_y}(x)^\dagger\sigma^x\Psi_{k_y}, \quad \text{(B3)}$$

$$\mathcal{H}_\Delta = \Delta\int_x \Psi_{k_y}(x)i\sigma^y\Psi_{-k_y}(x), \quad \text{(B4)}$$

$$\mathcal{H}_r = -\alpha_R k_y\int_x \Psi^\dagger_{k_y}\sigma^x\Psi_{k_y}, \quad \text{(B5)}$$

where we have introduced the spinor notation $\Psi_{k_y} = (\psi_{k_y,\uparrow}, \psi_{k_y,\downarrow})^T$. Next, we linearize the spectrum close to the Fermi points, see Fig. 8. The fields then take the form

$$\Psi_{k_y+}(x) = e^{-ik_{so}x}L_{k_y+}(x) + R_{k_y+}(x), \tag{B6}$$

$$\Psi_{k_y-}(x) = e^{ik_{so}x}R_{k_y-}(x) + L_{k_y-}(x), \tag{B7}$$

where $R_{k_y\sigma}(x)$ and $L_{k_y\sigma}(x)$ are slowly varying, and the spin-orbit eigenvectors of the bare Hamiltonian (B1) are given by $\Psi_{k_y-} = (i\sin\chi_k/2, \cos\chi_k/2)^T$, $\Psi_{k_y+} = (\cos\chi_k/2, i\sin\chi_k/2)^T$, with $b_k\cos\chi_k = \lambda_I k(k^2 - 3k_y^2)$ and $b_k\sin\chi_k = \alpha_R k$. Note that for strong Ising SOC the spins are aligned along the z direction $\tan\chi_k \to 0$.

Ignoring strongly oscillatory terms, the kinetic energy can be written as

$$\mathcal{H}_0 = -iv_i\int_x R^\dagger_{k_y+}(x)\partial_x R_{k_y+} - L^\dagger_{k_y-}(x)\partial_x L_{k_y-} \tag{B8}$$

$$-iv_e\int_x R^\dagger_{k_y-}(x)\partial_x R_{k_y-} - L^\dagger_{k_y+}(x)\partial_x L_{k_y+} \tag{B9}$$

and the gap-opening terms then become

$$\mathcal{H}_z = h\int_x R^\dagger_{k_y+}(x)L_{k_y-}(x) + \text{H.c.}, \tag{B10}$$

$$\mathcal{H}_\Delta = \Delta\int_x [R_{k_y+}(x)L_{-k_y-}(x) + L_{k_y+}(x)R_{-k_y-}(x)], \tag{B11}$$

$$\mathcal{H}_r = -\alpha_R k_y\int_x R^\dagger_{k_y+}(x)L_{k_y-}(x) + \text{H.c.}. \tag{B12}$$

The Hamiltonian separates into two decoupled subsystems, which we label the "external" (e) and "internal" (i) branches $\Phi_e = (L_{k_y+}, R_{k_y-}, L^\dagger_{-k_y+}, R^\dagger_{-k_y-})^T$ and $\Phi_i = (R_{k_y+}, L_{k_y-}, R^\dagger_{-k_y+}, L^\dagger_{-k_y-})^T$ with the respective Hamiltonians,

$$\mathcal{H}_i = -iv_i\partial_x\sigma^z + h\tau^z\sigma^x - \alpha_R k_y\sigma^x + \Delta\tau^y\sigma^y, \tag{B13}$$

$$\mathcal{H}_e = iv_e\partial_x\sigma^z + \Delta\tau^y\sigma^y. \tag{B14}$$

In what follows we will drop the subscript k_y for brevity.

We solve for a semi-infinite wire with a boundary at $x = 0$. We make the following ansatz for the zero mode, $\mathcal{H}_l\phi_l(x) = 0$ with $\phi_l(x) = e^{-x/\xi_l}\phi_l(0)$ where $l = e/i$ with $\xi_e = v_e/\Delta$ and two possible values ξ_i for the inner branch $\xi_{i1} = \frac{v_i}{h+\sqrt{\Delta^2+\alpha_R^2k_y^2}}$ and $\xi_{i2} = \frac{v_i}{h-\sqrt{\Delta^2+\alpha_R^2k_y^2}}$. Reincorporating the oscillatory phases and expressing the zero-mode solutions in terms of the original basis $\mathbf{\Psi} = (\Psi_{k_y+}, \Psi_{k_y-}, \Psi^\dagger_{-k_y+}, \Psi^\dagger_{-k_y-})^T$ we find

$$\psi_{i1} = \phi_{i1} = e^{-x/\xi_{i1}}\begin{pmatrix} -i \\ -1 \\ \frac{i}{\beta} \\ -\frac{1}{\beta} \end{pmatrix}, \tag{B15}$$

$$\psi_{i2} = \phi_{i2} = e^{-x/\xi_{i2}}\begin{pmatrix} i \\ 1 \\ +i\beta \\ -\beta \end{pmatrix}, \tag{B16}$$

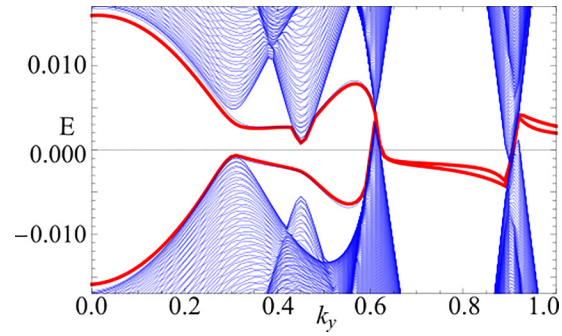

FIG. 9. Bulk and edge state spectrum for $\alpha = -0.01$, $\tilde{\mu} = -0.25$ $\mu_l = -0.175$, $m = 1$, $\lambda_{SO} = 0.15$, $h = 0.1$, and $\Delta = 0.06$. $\mu_l \neq 0$ on either of the two edges, breaks the reflection symmetry and lifts the degeneracy of the edge states (shown as solid red lines).

with $\beta = \frac{\alpha_R k_y - \sqrt{\Delta^2+\alpha_R^2k_y^2}}{\Delta}$ and

$$\psi_{e1} = e^{-x/\xi_e}\begin{pmatrix} ie^{-ik_{so}x} \\ e^{ik_{so}x} \\ -ie^{ik_{so}x} \\ e^{-ik_{so}x} \end{pmatrix}, \tag{B17}$$

$$\psi_{e2} = e^{-x/\xi_e}\begin{pmatrix} ie^{-ik_{so}x} \\ -e^{ik_{so}x} \\ ie^{ik_{so}x} \\ e^{-ik_{so}x} \end{pmatrix}. \tag{B18}$$

This allows us to construct a zero mode that satisfies the boundary conditions at $x = 0$ namely $\psi_M(x = 0) = 0$, which is

$$\begin{aligned}\psi_M(x) &= \frac{\beta(\beta+1)}{\beta-1}\psi_{i1} + \psi_{i2} + \frac{(\beta^2+1)}{\beta-1}\psi_{e1} \\ &= \frac{\beta(\beta+1)}{\beta-1}e^{-x/\xi_{i1}}\begin{pmatrix} -i \\ -1 \\ \frac{i}{\beta} \\ -\frac{1}{\beta} \end{pmatrix} + e^{-x/\xi_{i2}}\begin{pmatrix} i \\ 1 \\ +i\beta \\ -\beta \end{pmatrix} \\ &\quad + \frac{(\beta^2+1)}{\beta-1}e^{-x/\xi_e}\begin{pmatrix} ie^{-ik_{so}x} \\ e^{ik_{so}x} \\ -ie^{ik_{so}x} \\ e^{-ik_{so}x} \end{pmatrix}.\end{aligned} \tag{B19}$$

We note that in the absence of Rashba SOC, $\beta = -1$, and the boundary mode indeed satisfies the Majorana condition namely $\psi_M|_{\alpha_R=0} = (u_+(x), u_-(x), u^*_+(x), u^*_-(x))^T$. However, at finite $\alpha_R \neq 0$ this condition is no longer met and the boundary state is no longer a Majorana mode.

APPENDIX C: BREAKING OF REFLECTION SYMMETRY

In the family of 1D chains with open boundary conditions (15), the degeneracy of the midgap states is protected by mirror symmetry M_x, i.e., the edge states are reflected onto each other under this symmetry. Breaking the symmetry by adding a local potential on one of the two edges $\mu_l \neq \tilde{\mu}$ will lift the degeneracy. This situation is shown in Fig. 9.

Conversely, in the absence of Rashba SOC, i.e., when $\alpha_R = 0$ the degeneracy is protected by the chiral symmetry of the 1D chain for fixed k_y. Consequently, the degeneracy is not lifted even in the presence of a local chemical potential.

[1] B. T. Zhou, N. F. Q. Yuan, H.-L. Jiang, and K. T. Law, Ising superconductivity and Majorana fermions in transition-metal dichalcogenides, Phys. Rev. B **93**, 180501(R) (2016).

[2] S. Ilić, J. S. Meyer, and M. Houzet, Enhancement of the upper critical field in disordered transition metal dichalcogenide monolayers, Phys. Rev. Lett. **119**, 117001 (2017).

[3] W.-Y. He, B. T. Zhou, J. J. He, N. F. Q. Yuan, T. Zhang, and K. T. Law, Magnetic field driven nodal topological superconductivity in monolayer transition metal dichalcogenides, Commun. Phys. **1**, 40 (2018).

[4] E. Sosenko, J. Zhang, and V. Aji, Unconventional superconductivity and anomalous response in hole-doped transition metal dichalcogenides, Phys. Rev. B **95**, 144508 (2017).

[5] Y. Nakamura and Y. Yanase, Odd-parity superconductivity in bilayer transition metal dichalcogenides, Phys. Rev. B **96**, 054501 (2017).

[6] D. Möckli and M. Khodas, Robust parity-mixed superconductivity in disordered monolayer transition metal dichalcogenides, Phys. Rev. B **98**, 144518 (2018).

[7] M. H. Fischer, M. Sigrist, and D. F. Agterberg, Superconductivity without inversion and time-reversal symmetries, Phys. Rev. Lett. **121**, 157003 (2018).

[8] M. Smidman, M. B. Salamon, H. Q. Yuan, and D. F. Agterberg, Superconductivity and spin orbit coupling in noncentrosymmetric materials: A review, Rep. Prog. Phys. **80**, 036501 (2017).

[9] N. F. Q. Yuan, K. F. Mak, and K. T. Law, Possible topological superconducting phases of MoS_2, Phys. Rev. Lett. **113**, 097001 (2014).

[10] R. Oiwa, Y. Yanagi, and H. Kusunose, Theory of superconductivity in hole-doped monolayer MoS_2, Phys. Rev. B **98**, 064509 (2018).

[11] Y.-T. Hsu, A. Vaezi, M. H. Fischer, and E.-A. Kim, Topological superconductivity in monolayer transition metal dichalcogenides, Nat. Commun. **8**, 14985 (2017).

[12] L. Wang, T. O. Rosdahl, and D. Sticlet, Platform for nodal topological superconductors in monolayer molybdenum dichalcogenides, Phys. Rev. B **98**, 205411 (2018).

[13] R. Oiwa, Y. Yanagi, and H. Kusunose, Time-reversal symmetry breaking superconductivity in hole-doped monolayer MoS_2, J. Phys. Soc. Jpn. **88**, 063703 (2019).

[14] E. Sohn, X. Xi, W.-Y. He, S. Jiang, Z. Wang, K. Kang, J.-H. Park, H. Berger, L. Forró, K. T. Law *et al.*, An unusual continuous paramagnetic-limited superconducting phase transition in 2D $NbSe_2$, Nat. Mater. **17**, 504 (2018).

[15] Q. H. Wang, K. Kalantar-Zadeh, A. Kis, J. N. Coleman, and M. S. Strano, Electronics and optoelectronics of two-dimensional transition metal dichalcogenides, Nat. Nanotechnol. **7**, 699 (2012).

[16] A. K. Geim and I. V. Grigorieva, Van der Waals heterostructures, Nature (London) **499**, 419 (2013).

[17] J. M. Lu, O. Zheliuk, I. Leermakers, N. F. Q. Yuan, U. Zeitler, K. T. Law, and J. T. Ye, Evidence for two-dimensional Ising superconductivity in gated MoS_2, Science **350**, 1353 (2015).

[18] M. M. Ugeda, A. J. Bradley, Y. Zhang, S. Onishi, Y. Chen, W. Ruan, C. Ojeda-Aristizabal, H. Ryu, M. T. Edmonds, H.-Z. Tsai *et al.*, Characterization of collective ground states in single-layer $NbSe_2$, Nat. Phys. **12**, 92 (2016).

[19] Y. Saito, Y. Nakamura, M. S. Bahramy, Y. Kohama, J. Ye, Y. Kasahara, Y. Nakagawa, M. Onga, M. Tokunaga, T. Nojima *et al.*, Superconductivity protected by spin-valley locking in ion-gated MoS_2, Nat. Phys. **12**, 144 (2016).

[20] X. Xi, Z. Wang, W. Zhao, J.-H. Park, K. T. Law, H. Berger, L. Forró, J. Shan, and K. F. Mak, Ising pairing in superconducting $NbSe_2$ atomic layers, Nat. Phys. **12**, 139 (2016).

[21] D. Costanzo, S. Jo, H. Berger, and A. F. Morpurgo, Gate-induced superconductivity in atomically thin MoS_2 crystals, Nat. Nanotechnol. **11**, 339 (2016).

[22] T. Dvir, F. Massee, L. Attias, M. Khodas, M. Aprili, C. H. L. Quay, and H. Steinberg, Spectroscopy of bulk and few-layer superconducting $NbSe_2$ with van der Waals tunnel junctions, Nat. Commun. **9**, 598 (2018).

[23] S. C. de la Barrera, M. R. Sinko, D. P. Gopalan, N. Sivadas, K. L. Seyler, K. Watanabe, T. Taniguchi, A. W. Tsen, X. Xu, D. Xiao, and B. M. Hunt, Tuning Ising superconductivity with layer and spin-orbit coupling in two-dimensional transition-metal dichalcogenides, Nat. Commun. **9**, 1427 (2018).

[24] Y. Xing, K. Zhao, P. Shan, F. Zheng, Y. Zhang, H. Fu, Y. Liu, M. Tian, C. Xi, H. Liu *et al.*, Ising superconductivity and quantum phase transition in macro-size monolayer $NbSe_2$, Nano Lett. **17**, 6802 (2017).

[25] A. Hamill, B. Heischmidt, E. Sohn, D. Shaffer, K.-T. Tsai, X. Zhang, X. Xi, A. Suslov, H. Berger, L. Forró *et al.*, Two-fold symmetric superconductivity in few-layer $NbSe_2$, Nat. Phys. **17**, 949 (2021).

[26] N. F. Q. Yuan, B. T. Zhou, W.-Y. He, and K. T. Law, Ising superconductivity in transition metal dichalcogenides, arXiv:1605.01847.

[27] Y. Liu, Z. Wang, X. Zhang, C. Liu, Y. Liu, Z. Zhou, J. Wang, Q. Wang, Y. Liu, C. Xi, M. Tian, H. Liu, J. Feng, X. C. Xie, and J. Wang, Interface-induced Zeeman-protected superconductivity in ultrathin crystalline lead films, Phys. Rev. X **8**, 021002 (2018).

[28] C.-w. Cho, J. Lyu, T. Han, C. Y. Ng, Y. Gao, G. Li, M. Huang, N. Wang, and R. Lortz, Distinct nodal and nematic superconducting phases in the 2D Ising superconductor $NbSe_2$, arXiv:2003.12467v1.

[29] C.-w. Cho, J. Lyu, L. An, T. Han, K. T. Lo, C. Y. Ng, J. Hu, Y. Gao, G. Li, M. Huang, N. Wang, J. Schmalian, and R. Lortz, Nodal and nematic superconducting phases in $NbSe_2$ monolayers from competing superconducting channels, Phys. Rev. Lett. **129**, 087002 (2022).

[30] P. A. Frigeri, D. F. Agterberg, I. Milat, and M. Sigrist, Phenomenological theory of the s-wave state in superconductors without an inversion center, Eur. Phys. J. B **54**, 435 (2006).

[31] M. Kuzmanović, T. Dvir, D. LeBoeuf, S. Ilić, M. Haim, D. Möckli, S. Kramer, M. Khodas, M. Houzet, J. S. Meyer, M. Aprili, H. Steinberg, and C. H. L. Quay, Tunneling spectroscopy of few-monolayer $NbSe_2$ in high magnetic fields: Triplet superconductivity and Ising protection, Phys. Rev. B **106**, 184514 (2022).

[32] Y. X. Zhao and Z. D. Wang, Topological classification and stability of Fermi surfaces, Phys. Rev. Lett. **110**, 240404 (2013).

[33] S. Matsuura, P.-Y. Chang, A. P. Schnyder, and S. Ryu, Protected boundary states in gapless topological phases, New J. Phys. **15**, 065001 (2013).

[34] J. A. Galvis, L. Chirolli, I. Guillamón, S. Vieira, E. Navarro-Moratalla, E. Coronado, H. Suderow, and F. Guinea, Zero-bias conductance peak in detached flakes of superconducting $2H$-TaS_2 probed by scanning tunneling spectroscopy, Phys. Rev. B **89**, 224512 (2014).

[35] A. K. Nayak, A. Steinbok, Y. Roet, J. Koo, G. Margalit, I. Feldman, A. Almoalem, A. Kanigel, G. A. Fiete, B. Yan, Y. Oreg, N. Avraham, and H. Beidenkopf, Evidence of topological boundary modes with topological nodal-point superconductivity, Nat. Phys. **17**, 1413 (2021).

[36] R. Seshadri, M. Khodas, and D. Meidan, Josephson junctions of topological nodal superconductors, SciPost Phys. **12**, 197 (2022).

[37] D. Shaffer, J. Kang, F. J. Burnell, and R. M. Fernandes, Crystalline nodal topological superconductivity and Bogolyubov Fermi surfaces in monolayer $NbSe_2$, Phys. Rev. B **101**, 224503 (2020).

[38] A. Altland and M. R. Zirnbauer, Nonstandard symmetry classes in mesoscopic normal-superconducting hybrid structures, Phys. Rev. B **55**, 1142 (1997).

[39] Y. Tanaka, M. Sato, and N. Nagaosa, Symmetry and topology in superconductors—Odd-frequency pairing and edge states, J. Phys. Soc. Jpn. **81**, 011013 (2012).

[40] M. Haim, A. Levchenko, and M. Khodas, Mechanisms of in-plane magnetic anisotropy in superconducting $NbSe_2$, Phys. Rev. B **105**, 024515 (2022).

[41] T. L. Hughes, E. Prodan, and B. A. Bernevig, Inversion-symmetric topological insulators, Phys. Rev. B **83**, 245132 (2011).

[42] C.-K. Chiu, H. Yao, and S. Ryu, Classification of topological insulators and superconductors in the presence of reflection symmetry, Phys. Rev. B **88**, 075142 (2013).

[43] L. Fu and C. L. Kane, Josephson current and noise at a superconductor/quantum-spin-Hall-insulator/superconductor junction, Phys. Rev. B **79**, 161408(R) (2009).

[44] R. M. Lutchyn, J. D. Sau, and S. Das Sarma, Majorana fermions and a topological phase transition in semiconductor-superconductor heterostructures, Phys. Rev. Lett. **105**, 077001 (2010).

[45] K. Flensberg, F. von Oppen, and A. Stern, Engineered platforms for topological superconductivity and Majorana zero modes, Nat. Rev. Mater. **6**, 944 (2021).

[46] K. Laubscher and J. Klinovaja, Majorana bound states in semiconducting nanostructures, J. Appl. Phys. **130**, 081101 (2021).